PHOTONICS Research

Spatial and frequency multimode in the dressing parametric amplified multiwave mixing process

Xinghua Li, Ji Wu, Siqi Xiong, Mengting Chen, Hongye Yan, Zhiguo Wang, and Yanpeng Zhang*

Key Laboratory for Physical Electronics and Devices of the Ministry of Education & Shaanxi Key Laboratory of Information Photonic Technique, Xi'an Jiaotong University, Xi'an 710049, China
**Corresponding author: ypzhang@mail.xjtu.edu.cn*

Received 22 May 2019; revised 27 August 2019; accepted 11 October 2019; posted 14 October 2019 (Doc. ID 368173); published 27 November 2019

The quantum multimode of correlated fields is essential for future quantum-correlated imaging. Here we investigate multimode properties theoretically and experimentally for the parametric amplified multiwave mixing process. The multimode behavior of the signals in our system stems from spatial phase mismatching caused by frequency resonant linewidth. In the spatial domain, we observe the emission rings with an uneven distribution of photon intensity in the parametric amplified four-wave mixing process, suggesting different spatial modes. The symmetrical distribution of spatial spots indicates the spatial correlation between the Stokes and anti-Stokes signals. While in the frequency domain, the multimode character is reflected as multiple peaks splitting in the signals' spectrum. A novelty in our experiment, the number of multimodes both in the spatial and frequency domains can be controlled by dressing lasers by modifying the nonlinear susceptibility. Finally, we extend the multimode properties to the multiwave mixing process. The results can be applied in quantum imaging.

https://doi.org/10.1364/PRJ.7.001454

1. INTRODUCTION

Multimode properties of correlated fields play a significant role in increasing the information-carrying capacity of future quantum information processing [1,2] and in improving the resolution of quantum imaging [3–5]. Generally speaking, two types of photon modes are distinguished: one is a spatial mode that transverses to the direction of propagation (cross section and divergence); the other is a temporal mode that is defined in the direction of propagation (time and frequency). Multispatial mode effects in squeezed-light-enhanced interferometric gravitational wave detectors have been researched by Töyrä *et al.* [6] and localized multispatial mode quadrature squeezing has been observed by Embrey *et al.* [7]. The previous study has shown that many approaches for the generation of nonclassical multimode light, such as parametric downconversion in $\chi^{(2)}$ nonlinear crystals [4,8], are particularly suitable for the preparation of multimode photons because of its large emission bandwidth in the spatial frequency domain [9]. Another approach is an optical parametric oscillator operating continuously inside a cavity with degenerate transverse modes [10]. Different from the above methods, the nondegenerate four-wave mixing (FWM) process is another competitive candidate [11] in rubidium (Rb) vapor, which has no requirement for an optical cavity due to the embedded nonlinearity and spatial separation of the twin output fields [12]. In the absence of a cavity, no mode selection occurs, and spatially multimode twin beams can be generated with few optical aberrations. Moreover, it also could be applied to further multimode configurations such as cascaded FWM processes or six-wave mixing (SWM) processes [13], which have a wide application in quantum entangled imaging [9] and nonclassical squeezing states [14,15]. In this paper, we present a deep analysis of multimode spatial and frequency degrees of freedom in a parametric amplified multiwave mixing (MWM) process. Dressing lasers are used to modulate the phase-matching conditions and nonlinear susceptibilities in MWM processes. In the spatial domain, we observed an inhomogeneous intensity ring with light spots, and these light spots provide comprehensive evidence of different spatial multimodes in our system of MWM. In the spectral domain, the multimode appears as one nondegenerate signal peak that is split into multiple peaks by dressing lasers. Such a splitting process can be attributed to both internal and external dressing effects. These observed results are consistent with theoretical simulation.

2. EXPERIMENTAL SETUP AND BASIC THEORY

The experimental setup is displayed in Fig. 1(a) along with the signal detection scheme. A Rb cell is placed as a primary source of nonlinear interaction and parametric amplification among the employed laser beams under the spontaneous parametric FWM process. The corresponding energy level configuration is displayed in Fig. 1(b). In a three-energy level Λ-type configuration (in the red dashed frame) involving two hyperfine ground states of $5S_{1/2}$ [$F = 2(|0\rangle)$ and $F = 3(|1\rangle)$] and an excited state $5P_{3/2}(|2\rangle)$, a pumping laser $\boldsymbol{E}_1$ (frequency ω_1, wave vector $\boldsymbol{k}_1$, Rabi frequency G_1, vertical polarization) is

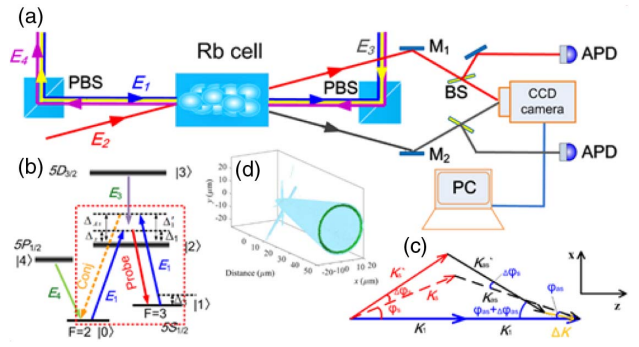

Fig. 1. (a) Experimental setup. PBS, polarized beam splitter; BS, beam splitter; M, mirror; APD, avalanche photodiode. (b) Energy diagram; (c) phase-mismatching diagram; (d) emission cone of Stokes.

set as 780.237 nm with power up to 100 mW. By applying a pump beam $\boldsymbol{E}_1$ in the said configuration, a spontaneous parametric FWM process happens and generates a pair of Stokes (ω_s) and anti-Stokes (ω_{as}) signals [16]. These two generated signals are spatially symmetric to the axis of pump beam $\boldsymbol{E}_1$ with an angle of 0.26° [Fig. 1(a)], satisfying the phase-matching conditions $\boldsymbol{k}_s = 2\boldsymbol{k}_1 - \boldsymbol{k}_{as}$ and $\boldsymbol{k}_{as} = 2\boldsymbol{k}_1 - \boldsymbol{k}_s$. When a weak probe laser $\boldsymbol{E}_2$ ($\omega_p, \boldsymbol{k}_p, G_p$, horizontal polarization, 400 μW) intersects with an $\boldsymbol{E}_1$ laser inside the Rb cell with the same angle of 0.26° and the same frequency as the Stokes or anti-Stokes signal ($\omega_p = \omega_s$ or $\omega_p = \omega_{as}$), the $\boldsymbol{E}_2$ laser could be treated as an injection into the Stokes or anti-Stokes signal channel; thus the Stokes or anti-Stokes signal could be amplified and form the parametric-amplified FWM process (PA-FWM). Next, another laser $\boldsymbol{E}_3$ ($\omega_3, \boldsymbol{k}_3, G_3$, a wavelength of 776 nm, vertically polarized) connects the energy transition $5P_{3/2}(|2\rangle)$ to $5D_{5/2}(|3\rangle)$ and forms an inverted Y-type energy level configuration. With the introduction of $\boldsymbol{E}_3$, the parametric-amplified six-wave mixing (PA-SWM) process could happen if the lasers $\boldsymbol{E}_1, \boldsymbol{E}_2$, and $\boldsymbol{E}_3$ are satisfying phase matching conditions $\boldsymbol{k}_{s1} = 2\boldsymbol{k}_1 - \boldsymbol{k}_{s2} - \boldsymbol{k}_3 + \boldsymbol{k}_{s3}$ and $\boldsymbol{k}_{s2} = 2\boldsymbol{k}_1 - \boldsymbol{k}_{s1} - \boldsymbol{k}_3 + \boldsymbol{k}_{s3}$. Similarly, laser $\boldsymbol{E}_4$ ($\omega_4, \boldsymbol{k}_4, G_4$, wavelength of 794. 97 nm, vertically polarized) acts as an external dressing laser for the SWM process. While in the eight-wave mixing (EWM) process, the phase-matching condition can be expressed by $\boldsymbol{k}_{s1} = 2\boldsymbol{k}_1 - \boldsymbol{k}_{s2} - \boldsymbol{k}_3 + \boldsymbol{k}_{s3} + \boldsymbol{k}_4 - \boldsymbol{k}_{s4}$ and $\boldsymbol{k}_{s2} = 2\boldsymbol{k}_1 - \boldsymbol{k}_{s1} - \boldsymbol{k}_3 + \boldsymbol{k}_{s3} + \boldsymbol{k}_4 - \boldsymbol{k}_{s4}$. It should be clarified that $\boldsymbol{E}_3$ and $\boldsymbol{E}_4$ lasers are treated as external dressing fields for the FWM process in the following analysis.

In the signal detection scheme, the Stokes and anti-Stokes signals generated by the FWM process are separated into two channels by a beam splitter (BS), and one channel is detected by an avalanche photodiode (APD) to obtain the spectrum, while the other channel is connected to a charge-coupled device (CCD) camera for the spatial images. The CCD camera is monitored by a computer. In the SWM detection process, the detection angle of S_1 and S_2 signals is nearly the same as those of the Stokes and anti-Stokes signals in the FWM process, while the output direction of the S_3 signal is along the z axis, which cannot be separated from the pumping beam. A similar occasion happens in EWM configuration: the S_3 and S_4 signals also cannot be detected; only S_1 and S_2 can be detected. We will improve the experimental scheme in future work.

For generating a nonclassical FWM signal, the pump beam $\boldsymbol{E}_1$ and probe beam $\boldsymbol{E}_2$ are coming from the same Ti:sapphire laser, and the probe laser frequency is shifted 3 GHz by an acousto-optic modulator (AOM) and then injected into the probe channel. They couple with the Λ-type atomic system in a naturally abundant Rb vapor cell. Then the PA-FWM process happens. The dressing fields of $\boldsymbol{E}_3$ and $\boldsymbol{E}_4$ are provided by two Toptica lasers. When $\boldsymbol{E}_4$ (795 nm, 4 mW) is added to $\boldsymbol{E}_1$ (in the same direction) and $\boldsymbol{E}_3$ (776 nm, 8 mW) counterpropagates with $\boldsymbol{E}_1$, they establish two electromagnetically induced transparency windows in the system and significantly modify (dress) the original PA-FWM process. Their frequencies are locked, but phases are unlocked. Subsequently, the output probe and conjugate beams are connected to a CCD camera for the spatial images [shown in Section 3, Figs. 5(a)–5(c)], which are nonclassical signals. It should be noted that, the phases of $\boldsymbol{E}_1$ and $\boldsymbol{E}_2$ are nonessential, locked for detecting the spectrum signal. For the intensity difference squeezing (IDS) measurements, the output probe and conjugate beams are detected by two balanced photodetectors; then the difference of the two detected signals is sent to a radio-frequency spectrum analyzer with a resolution bandwidth of 300 kHz and a video bandwidth of 10 kHz. The two mode-squeezing results have been published in Ref. [17].

For the SWM nonclassical experiment process, it occurs with the four-level "inverted-Y" type configuration. A strong pumping laser $\boldsymbol{E}_1$ (780 nm) and a weak probe beam $\boldsymbol{E}_2$ (780 nm) are generated from a cw Ti:sapphire laser. The weak probe beam $\boldsymbol{E}_2$ is applied to an AOM and its frequency shifts; it propagates in the $\boldsymbol{E}_1$ direction with an angle of 0.5° along the horizontal plane. Next, another laser $\boldsymbol{E}_3$ (776 nm) is applied to the system, and its phase is locked with pump beam $\boldsymbol{E}_1$. When the input beams satisfy the phase-matching condition $2\boldsymbol{k}_1 + \boldsymbol{k}_3 = \boldsymbol{k}_{s1} + \boldsymbol{k}_{s2} + \boldsymbol{k}_{s3}$, the SWM process could occur spontaneously. When the $\boldsymbol{E}_2$ is injected to the S_1 signal channel, the SWM parametric amplified process happens, and the three output lights S_1, S_2, and S_3 could be generated. The spatial light spots are shown in Section 3, Figs. 6(a)–6(c). In the future, we will continue to do the three-mode squeezing experiment.

A. Theoretical Estimation of the Parametric Gain Process

In order to ensure high chances of amplified output signal detection, a probe laser is injected into the Stokes channel with the matched frequency. However, in a parametric interaction of the FWM process, only photons generated in phase-matched modes lead to amplification. Under the undepleted pump approximation, the mean number of photons at the output of the medium can be expressed by [18]

$$G = (\gamma\Gamma)^2, \tag{1}$$

where γ can be defined by

$$\gamma = \frac{g}{K}\begin{cases} g > \frac{\Delta k}{2}, & K = \sqrt{g^2 - \left(\frac{\Delta k}{2}\right)^2}, \quad \Gamma = \sinh(KL) \\ g < \frac{\Delta k}{2}, & K = \sqrt{\left(\frac{\Delta k}{2}\right)^2 - g^2}, \quad \Gamma = \sin(KL) \end{cases}. \tag{2}$$

The phase mismatch term Δk is given by $\Delta k = 2k_1 - k_s\cos(\varphi_s) - \sqrt{k_{as}^2 - k_s^2[1-\cos^2(\varphi_s)]}$, and φ_s is the angle between Stokes and the z axis. The Stokes and anti-Stokes gain factor g is proportional to the nonlinear coupling coefficients κ, which is also directly proportional to third-order nonlinear susceptibility $\chi^{(3)}$. The $\chi^{(3)}$ can be obtained from the corresponding density matrix elements as $\chi_s^{(3)} = \left(N\mu_{20}^2\mu_{21}^2\rho_s^{(3)}\right)/\left(\varepsilon_0\hbar^3 F G_1 G_2 G_{as}\right)$ and $\chi_{as}^{(3)} = \left(N\mu_{20}^2\mu_{21}^2\rho_{as}^{(3)}\right)/(\varepsilon_0\hbar^3 F G_1 G_2 G_s)$, where N is the density of atoms, ε_0 is permittivity, μ_{ij} is the transition dipole moment between the levels $|i\rangle$ and $|j\rangle$, and $G_i = \mu_{ij}E_i/\hbar$ is the Rabi frequency for the laser $\boldsymbol{E}_i$. The density matrix elements for Stokes $\rho_{21(s)}^{(3)}$ and anti-Stokes $\rho_{20(as)}^{(3)}$ can be expressed by Eqs. (3) and (4), respectively. So, we can make an approximate treatment that the gain is proportional to $|\rho_{21(s)}^{(3)}|$ or $|\rho_{20(as)}^{(3)}|$, which can be calculated from the perturbation chain [19] $\rho_{11}^{(0)} \xrightarrow{\omega_1} \rho_{21}^{(1)} \xrightarrow{\omega_{as}} \rho_{01}^{(2)} \xrightarrow{\omega_1} \rho_{21(s)}^{(3)}$ (Stokes) or $\rho_{00}^{(0)} \xrightarrow{\omega_1} \rho_{20}^{(1)} \xrightarrow{\omega_s} \rho_{10}^{(2)} \xrightarrow{\omega_1} \rho_{20(as)}^{(3)}$ (anti-Stokes). The third-order nonlinear susceptibility of $\chi_s^{(3)}$ and $\chi_{as}^{(3)}$ can be written as

$$\chi_s^{(3)} = \frac{N\mu_{20}^2\mu_{21}^2}{\varepsilon_0\hbar^3(\Gamma_{21}+i\Delta_1')D_1D_2}, \tag{3}$$

$$\chi_{as}^{(3)} = \frac{N\mu_{20}^2\mu_{21}^2}{\varepsilon_0\hbar^3(\Gamma_{20}+i\Delta_1)D_1'D_2'}, \tag{4}$$

where Δ_1, Δ_1' are pumping laser detuning and defined as $\Delta_1 = \omega_{20} - \omega_1$, $\Delta_1' = \omega_{21} - \omega_1$, respectively. Δ_3 and Δ_4 are the frequency detuning of $\boldsymbol{E}_3$ and $\boldsymbol{E}_4$, respectively. $D_1 = \Gamma_{01} + i\delta + \frac{G_4^2}{\Gamma_{04}+i\delta+i\Delta_4}$, $D_2 = \Gamma_{21} + i\delta + i\Delta_1 + \frac{G_4^2}{\Gamma_{31}+i(\delta+\Delta_1+\Delta_3)}$, $D_1' = \Gamma_{21} + i\delta + i\Delta_1 + \frac{G_4^2}{\Gamma_{31}+i(\delta+\Delta_1+\Delta_3)}$, $D_2' = \Gamma_{20} - i\delta + i\Delta_1' + \frac{G_3^2}{\Gamma_{30}-i(\delta-\Delta_1'-\Delta_3)}$, and G_i is defined as laser Rabi frequency. Γ_{ij} denotes the dephasing rates of coherence energy level $|i\rangle \to |j\rangle$. δ is the signal fields' resonance linewidth corresponding to its central frequency.

Next, we come to the analysis of the gain factor g of the SWM process, which happens in the inverted Y-type energy level configuration [Fig. 1(b)], where laser $\boldsymbol{E}_4$ acts as an external dressing laser connecting energy level $|4\rangle \to |0\rangle$. The system gain factor g is proportional to the fifth-order density matrix elements $|\chi_{S_1}^{(5)}|$ and $|\chi_{S_2}^{(5)}|$ of S_1 and S_2 signals, respectively, and can be expressed as

$$\chi_{S_1}^{(5)} = \frac{N\mu_{20}\mu_{20}\mu_{21}\mu_{21}\mu_{32}\mu_{32}}{\varepsilon_0\hbar^5(\Gamma_{21}+i\Delta_2)(\Gamma_{31}+i\Delta_2+i\Delta_3)d_1d_2d_3}, \tag{5}$$

$$\chi_{S_2}^{(5)} = \frac{N\mu_{20}\mu_{20}\mu_{21}\mu_{21}\mu_{32}\mu_{32}}{(\Gamma_{20}+i\Delta_1)(\Gamma_{30}-i\delta_1+i\Delta_1'+i\Delta_3)d_1'd_2'd_3'}, \tag{6}$$

where d_1, d_2, d_3, d_1', d_2', and d_3' can be defined by $d_1 = \Gamma_{21} + i\delta_1 + i\Delta_1 + \frac{G_1^2}{\Gamma_{01}+i\delta_1}$, $d_2 = \Gamma_{21} - i\delta_2 + i\Delta_2 + \frac{G_3^2}{\Gamma_{31}+i\Delta_2-i\delta_2+i\Delta_3}$, $d_3 = \Gamma_{01} + i\delta_1 + \frac{G_4^2}{\Gamma_{41}+i\delta_1+i\Delta_4}$, $d_1' = \Gamma_{20} - i\delta_1 + i\Delta_1' - i\delta_3 + \frac{G_1^2}{\Gamma_{00}-i\delta_1-i\delta_3}$, $d_2' = \Gamma_{20} - i\delta_1 + i\Delta_1' + \frac{G_1^2}{\Gamma_{30}-i\delta_1+i\Delta_1'+i\Delta_3}$, and $d_3' = \Gamma_{10} - i\delta_1 + \frac{G_4^2}{\Gamma_{14}-i\delta_1-i\Delta_4}$, respectively.

B. Frequency Mode Analysis

Based on the third-order nonlinear susceptibility in Eqs. (3) and (4), we begin with the case of frequency multimode through FWM. Here only pump beam $\boldsymbol{E}_1$ and probe beam $\boldsymbol{E}_2$ interact inside the Rb vapor, which forms a PA-FWM process. External lasers $\boldsymbol{E}_3$ and $\boldsymbol{E}_4$ are applied to the system as dressing lasers to modify the nonlinear susceptibility. For the sake of frequency multimode, the frequency linewidth δ is introduced in calculation of $\chi^{(3)}$, which causes the wave vector $\boldsymbol{k}$ to change in scale in a spatial degree of freedom as $k = \omega_i n_i/c$; n_i represents the reflective index. ω_i is defined as the actual frequency of Stokes (anti-Stokes), which is assumed as $\omega_s = \varpi_s + \delta$ ($\omega_{as} = \varpi_{as} - \delta$) as per the energy conservation law in the FWM process; ϖ_s and ϖ_{as} denote the central frequency of Stokes and anti-Stokes signals, respectively. Then the phase mismatching Δk in the z axis and x axis components can be expressed by Eqs. (7) and (8), respectively,

$$\Delta k_z = \frac{1}{c}[2\omega_1 n_1 - (\varpi_s+\delta)n_s\cos(\varphi_s) - (\varpi_{as}-\delta)n_{as}\cos(\varphi_{as})], \tag{7}$$

$$\Delta k_x = \frac{1}{c}[(\varpi_s+\delta)n_s\sin(\varphi_s) + (\varpi_{as}-\delta)n_{as}\sin(\varphi_{as})]. \tag{8}$$

The equations show the relationship between Δk and δ. The frequency linewidth δ locates in the range $\omega_s[\cos(\varphi_s) - 1] < \delta < \omega_{as}[1 - \cos(\varphi_{as})]$, which determines the maximum tolerance of phase mismatching. So, getting the exact values of resonance frequency δ is very important for quantitative analysis of phase mismatching. On the other hand, the resonance position will determine how many frequency modes can be generated for the Stokes and anti-Stokes signals and how these modes are correlated with each other and the generation mechanisms behind the FWM processes [20]. By analysis of the nonlinear susceptibilities in Eqs. (3) and (4), we can get the exact roots of resonance frequency δ of Stokes and anti-Stokes. Taking the nonlinear susceptibility of Stokes without the external dressing effect, for example, and setting the whole denominator of Eq. (3) equal to zero, we can get two roots $\delta_1 = 0 + i\Gamma_{01}$ and $\delta_2 = \Delta_1 + i\Gamma_{21}$. The real part of the roots denotes the maxima of the resonances, whereas the imaginary part denotes the full width at half-maximum (FWHM) of the resonance peak. These two resonances correspond to two FWM processes existing in the system. The first FWM process happens when the Stokes mode is centered at $\varpi_s + 0$, and the anti-Stokes mode is centered at $\varpi_{as} - 0$. The second FWM occurs as the Stokes mode peaks at $\varpi_s + \Delta_1$, while the anti-Stokes mode peaks at $\varpi_{as} - \Delta_1$. As per expectation, both the FWMs satisfy the energy conservation $2k_1 - \omega_s - \omega_{as} = 0$. Further, the simulation of nonlinear susceptibility of Stokes and anti-Stokes versus δ without external dressing laser $\boldsymbol{E}_3$ is shown in Figs. 2(a1) and 2(a2), respectively. The results show that both Stokes and anti-Stokes signals have two maxima. The modes in Figs. 2(a1) and 2(a2) marked in same number have correlation performance like that in Ref. [21]. When the external dressing laser $\boldsymbol{E}_3$ is turned on, we can get three

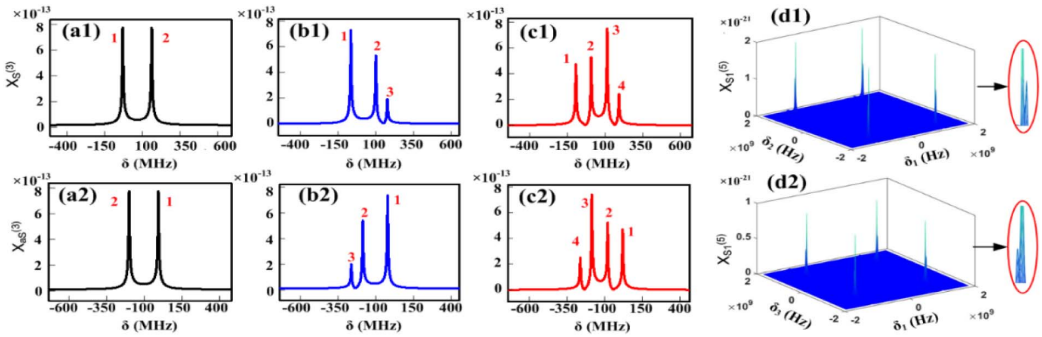

Fig. 2. Third-order nonlinear susceptibility of Stokes and anti-Stokes signals versus frequency linewidth δ obtained from FWM; (a1), (a2) without dressing effect; (b1), (b2) with $\boldsymbol{E}_3$ field single-dressing effect; (c1), (c2) with $\boldsymbol{E}_3$ and $\boldsymbol{E}_4$ double-dressing effect; (d1), (d2) fifth-order nonlinear susceptibility versus frequency linewidth δ obtained in SWM, $\delta_1 + \delta_2 + \delta_3 = 0$.

maxima for Stokes and anti-Stokes signals from the numerical simulations of frequency resonances δ versus nonlinear susceptibility, shown in Figs. 2(b1) and 2(b2), respectively. The exact roots of δ are $\delta = 0$, $\delta = \frac{(-\Delta_3-2\Delta_2)+\sqrt{\Delta_3^2+4G_3^2+4\Gamma_{21}\Gamma_{31}}}{2}$, and $\delta = \frac{(-\Delta_3-2\Delta_2)-\sqrt{\Delta_3^2+4G_3^2+4\Gamma_{21}\Gamma_{31}}}{2}$. Furthermore, both the external dressing lasers $\boldsymbol{E}_3$ and $\boldsymbol{E}_4$ are turned on, and Figs. 2(c1) and 2(c2) display four resonant peaks of Stokes and anti-Stokes, respectively. These simulation results suggest more frequency modes in FWMs caused by the dressing effect.

A similar analysis method is used in the case of the SWM process, which happens in the inverted Y-type configuration. Two dependent variables, δ_1 and δ_2, are introduced into $\chi^{(5)}$, the nonlinear susceptibility presented in Eqs. (5) and (6). The exact roots of δ_1 and δ_2 are $\delta_{2\pm} = \frac{(\Delta_3+2\Delta_2)\pm\sqrt{\Delta_3^2+4G_1^2+4\Gamma_{21}\Gamma_{31}}}{2}$, $\delta_{1\pm} = \frac{-\Delta_1\pm\sqrt{\Delta_1^2+4G_1^2+\Gamma_{21}\Gamma_{01}}}{2}$, and $\delta_{1\pm} = \frac{-\Delta_4\pm\sqrt{\Delta_4^2+4G_4^2+\Gamma_{41}\Gamma_{01}}}{2}$, respectively. Then the actual frequencies of the S_1, S_2, and S_3 signals can be expressed by $\omega_{S_1} = \varpi_{S_1} + \delta_1$, $\omega_{S_2} = \varpi_{S_2} + \delta_2$, and $\omega_{S_3} = \varpi_{S_3} - \delta_1 - \delta_2$, respectively. Figures 2(d1) and 2(d2) show the simulation of the SWM nonlinear susceptibility from Eqs. (5) and (6), respectively. Four resonant peaks suggest there are four SWM processes coexisting and each of the resonance splits into two peaks [partial enlargement of Figs. 2(d1) and 2(d2)] if considering the internal dressing lasers $\boldsymbol{E}_1, \boldsymbol{E}_3$. This splitting process indicates more frequency modes in the SWM system. The SWM phase mismatching Δk in the z axis and x axis components can be expressed by Eqs. (9) and (10), respectively,

$$\begin{aligned}\Delta k_z = \frac{1}{c}\{&2\omega_1 n_1 - \omega_3 - (\varpi_{S_1} + \delta_1)n_{S_1}\cos(\varphi_{S_1}) \\ &- (\varpi_{S_2} + \delta_2)n_{S_2}\cos(\varphi_{S_2}) \\ &+ [\varpi_{S_3} - (\delta_1 + \delta_2)]n_{S_3}\cos(\varphi_{S_2})\},\end{aligned} \tag{9}$$

$$\begin{aligned}\Delta k_x = &(\varpi_{S_1} + \delta_1)n_{S_1}\sin(\varphi_{S_1}) - (\varpi_{S_2} + \delta_2)n_{S_2}\sin(\varphi_{S_2}) \\ &- [\varpi_{S_3} - (\delta_1 + \delta_2)]n_{S_3}\sin(\varphi_{S_3}).\end{aligned} \tag{10}$$

Here, we define φ_{S_1}, φ_{S_2}, and φ_{S_3} as the angle between the S_1, S_2, and S_3, and z axis, respectively. When extending to the EWM process, four photons are generated by the $\chi^{(7)}$ nonlinear process. Three dependent variables (δ_1, δ_2, and δ_3) are introduced to the $\chi^{(7)}$ expression for calculation. We also predict the number of resonant frequencies in the EWM process. Table 1 lists the number of resonant frequency modes in FWM, single-dressing FWM (SFWM), double-dressing FWM (DFWM), SWM, dressing SWM (DSWM), and the EWM process.

Table 1. Number of Resonant Frequency Modes in MWM Process

	FWM	SFWM	DFWM	SWM	DSWM	EWM
S_1	2	3	4	2	4	2
S_2	2	3	4	4	8	2
S_3	–	–	–	2	2	2
S_4	–	–	–	–	–	8

C. Spatial Mode Analysis

In this part, we focus on the number of spatial modes theoretically, which can be expressed by Eq. (11),

$$N_{\text{spacial}} = \frac{\text{PM}_{\text{area}}}{\text{Spacial mode size}}, \tag{11}$$

where the phase-matching area (PM_{area}) can be calculated by the solid angle $\Delta\Omega = \pi\Delta\Phi^2$, with $\Delta\Phi$ being the maximum internal angle of the signal. The solid angle where fluorescence attains 44% of its maximum value is given by Eq. (12) [9],

$$\Delta\Omega = \pi\Delta\Phi^2 = \pi\frac{\Delta k}{|k_1|}. \tag{12}$$

From Eq. (12), we can see that the phase mismatching Δk is related to the solid angle, which plays a crucial role in the number of spatial modes. So in the following, we present Δk with detailed analysis. In the FWM process, the simple case is the perfect phase-matching configuration $\Delta k = 0$ (corresponding to the optimal phase-matching angle), meaning the beams are completely phase-matched, which leads to the largest efficiency to generate the FWMs on the phase-matching ring. However, the number of spatial modes is nearly equal to zero according to Eqs. (11) and (12). Figure 3(a1) shows the ideal Stokes cone under a perfect phase-matching condition in the FWM process. The anti-Stokes cone is nearly overlapped with a Stokes cone, so it is not being put here. Figure 3(a2) shows the simulation

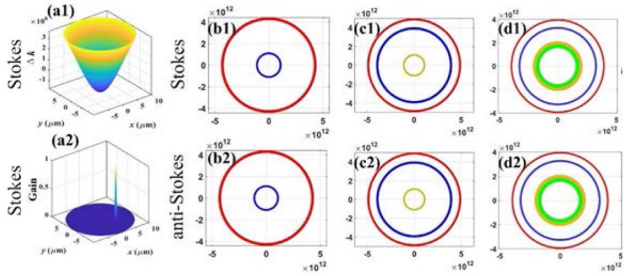

Fig. 3. (a1) In FWM process, the emission cone of Stokes signal; (a2) parametric amplified Stokes signal. The cross section of Stokes and anti-Stokes signals in FWM: (b1), (b2) without $\boldsymbol{E}_3$ laser dressing; (c1), (c2) with $\boldsymbol{E}_3$ laser dressing; (d1), (d2) with $\boldsymbol{E}_3$ and $\boldsymbol{E}_4$ lasers' double dressing.

results of parametric amplified Stokes signal, and a very few of modes are amplified because of the small tolerance of the phase-matching condition.

Next, we focus on the phase-mismatching case $\Delta k \neq 0$. In Eqs. (7) and (8), the relaxation of the phase-mismatching condition stems from the FWHM of the Stokes and anti-Stokes frequency resonance peak, which brings about the spatial deviation of k both in the x axis and the z axis. The transverse component (x axis) of Stokes causes the emission cone having a thickness in a spatial degree of freedom [Fig. 1(d)]. The phase-mismatching schematic is shown in Fig. 1(c). Figures 3(b1) and 3(b2) show the simulation results of the Stokes and anti-Stokes signals, respectively, at a certain cross section of the pump axis. Both signals have two rings that correspond to two central spatial modes. The ring width represents the maximum tolerance of mismatching and the generation coefficient decreasing sharply when deviating from this ring. By considering external dressing laser $\boldsymbol{E}_3$, three rings emerge for both signals due to dressing energy level splitting. As expected, when considering the $\boldsymbol{E}_3$ and $\boldsymbol{E}_4$ lasers' double-dressing effect, both the Stokes and anti-Stokes signals have four rings, corresponding to the four central spatial modes [Figs. 3(d1) and 3(d2)]. It indicates dressing lasers will result in a large possibility of spatial multimode.

Following that, Figs. 4(a1)–4(a3) show the cross section of S_1, S_2, and S_3 emission cones in SWM, respectively.

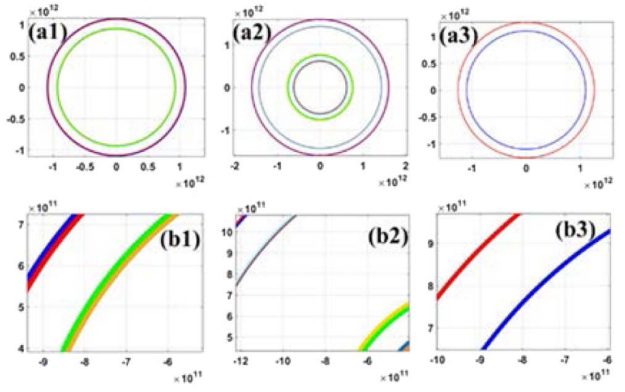

Fig. 4. (a1)–(a3) Cross sections of S_1, S_2, and S_3 signals cone in SWM with $\boldsymbol{E}_3$ and $\boldsymbol{E}_4$ lasers' dressing; (b1)–(b3) partial enlargements of (a1), (a2), and (a3), respectively.

Table 2. Number of Central Spatial Modes for Each Signal in MWM Process

	FWM	SFWM	DFWM	SWM	DSWM	EWM
S_1	2	3	4	2	4	2
S_2	2	3	4	4	8	2
S_3	–	–	–	2	2	2
S_4	–	–	–	–	–	8

Obviously, more rings arise in each signal compared to that in FWM process, suggesting the potential of SWM carrying more modes than the FWM process. However, the ring width is narrower compared to that of FWM [Figs. 4(b1)–4(b3)], indicating the SWM process needs a stricter phase-matching condition compared to that of the FWM process. Table 2 lists the number of central spatial modes for each signal in the MWM process. It should be noted that the phase-matching configuration of SWM in our experiment is a specific case: the k_{s3} is along the z axis, and it does not have a component in the x axis, so the S_3 signal does not have spatial transverse modes; only S_1 and S_2 signals have spatial modes.

As we know, the spatial modes of correlation photons are useful in ghost imaging [22]. According to our experimental geometric scheme in Fig. 1(a), the biphoton image of FWM is reversed because the transverse momentum of Stokes and anti-Stokes signals is anticorrelated and satisfies the condition $\boldsymbol{k}_{xs1} + \boldsymbol{k}_{xs2} = 0$ ($k_{xs1} - k_{xs2} = 0$ scalar). When extending to the MWM process, the photons' transverse momentum of SWM satisfies $\boldsymbol{k}_{xs1} + \boldsymbol{k}_{xs2} + \boldsymbol{k}_{xs3} = 0$ ($k_{xs1} - k_{xs2} + k_{xs3} = 0$ scalar). These correlated triphotons also can be applied in improving the image information. When S_1 photons and S_3 photons pass through the object, and S_2 photons pass through the imaging, it can get a reversed image because the sum momentum of S_1 and S_3 is anti-correlated with the S_2 photons' momentum, while for the quadphoton of the EWM process, their transverse momentum satisfies the condition $\boldsymbol{k}_{xs1} + \boldsymbol{k}_{xs2} + \boldsymbol{k}_{xs3} + \boldsymbol{k}_{xs4} = 0$ ($k_{xs1} - k_{xs2} + k_{xs3} - k_{xs4} = 0$ scalar). It has many imaging possibilities. One case is that S_1 acts as trigger, with S_2 and S_4 photons passing through the object at the same time when S_3 photons pass through the image. The image is reversed as the sum momentum of S_2 and S_4 is anticorrelated by that of S_3.

Briefly, provided that the probe laser $\boldsymbol{E}_2$ is not injected into the Stokes or anti-Stokes channel, then each pair of correlated Stokes and anti-Stokes photons could distribute evenly between the ideal Stokes and anti-Stokes cones. So, at a certain cross section of the pump axis, the intensity of photons appears evenly on a circular ring. The larger number of spatial modes caused by the dressing laser is reflected in the increasing number of spatial rings. Therefore, it can be proved that the MWM process will have more potential to generate more spatial multimodes.

3. EXPERIMENTAL RESULTS

After a theoretical detail analysis of multimode, next, we will emphasize experimental results. When applying an injecting laser to a system, the intensities of signals are amplified with multiples of gain, which provides a better chance for detection. However, the spatial multimode distribution is unaffected.

In the PA-FWM process, the probe field $\boldsymbol{E}_2$ is injected into the Stokes channel when its frequency detuning Δ_2 is set at $\Delta_2 = \Delta_s$, where Δ_s is defined as the frequency detuning of the Stokes signal. Figures 5(a1)–5(a6) show the evolution of spatial images versus pumping laser frequency detuning Δ_1 from −500 to 500 MHz. The shape of the anti-Stokes spatial images shows a ring around the pump beam direction and exhibits intensity inhomogeneity. First, at $\Delta_1 = -500$ MHz, the light intensity in the rings has few bright spots; later, more spots appear subsequently as Δ_1 approaches resonance. These spots gradually become weak and disappear as the laser's detuning is getting away from resonance. The different response of these spots number to Δ_1 suggests different spatial modes. So instead of using a noise figure (NF) [23], we prove spatial multimode by carefully analyzing the details of light spot images. The Stokes signal is not put here because it nearly overlaps with the anti-Stokes signal. Moreover, the ring approaches integrity with the medium temperature increasing, shown in Figs. 5(a)–5(c). In addition, the light spots are symmetrically distributed, indicating the spatial correlation of Stokes and anti-Stokes signals, which are outlined by the red dashed circle in Figs. 5(b3) and 4(b4).

Next, we begin spectral analysis of multimode in the PA-FWM process. Figure 5(d1) shows the intensity change of the anti-Stokes signal versus the spot radius of the pumping laser. The anti-Stokes signal splits into two peaks because of the energy level splitting ($|2\rangle\, 5P_{2/3}$) induced by intensive pump fields, which is the so-called Autler–Townes splitting [24]. Multiple split peaks are direct evidence of multimode in the frequency domain. Specifically, when the external laser $\boldsymbol{E}_3$ is applied to the system, the dressing anti-Stokes signal exhibits a suppression dip [25] by scanning the dressing laser's detuning [Fig. 5(d2)]. In the theory part above, we simulated the anti-Stokes and Stokes optical response versus the frequency linewidth δ. In Fig. 2(b2), the anti-Stokes signal has two maxima under the influence of internal dressing; then one of these two maxima further splits into two maxima under the influence of an introduced external dressing laser. The experimental results in Fig. 5(d1) fit perfectly with our theoretical prediction.

After the discussion about multimode in PA-FWM, in Fig. 6, we study the spatial and frequency multimode of the PA-SWM process. In our experimental configuration, the output direction of S_3 is along the z axis according to the phase-matching condition $k_{s1} = 2k_1 - k_{s2} - k_3 + k_{s3}$, which cannot be separated from the pumping beam. So, only S_1 and S_2 signals can be detected here. In the future, we will improve the experimental scheme. When the probe beam is injected

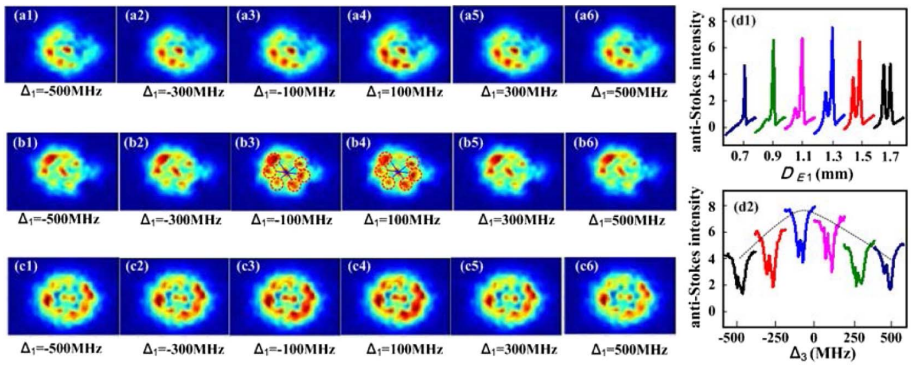

Fig. 5. In PA-FWM process, evolutions of the generated anti-Stokes signals' spatial images captured by discretely modifying pumping frequency detuning Δ_1. (a1)–(a6) Rb temperature is 55°C; (b1)–(b6) Rb temperature is 70°C; (c1)–(c6) Rb temperature is 85°C; (d1) frequency spectrum of anti-Stokes versus pumping frequency detuning Δ_1 at different diameters D of pump beam $\boldsymbol{E}_1$; (d2) frequency spectrum of anti-Stokes versus external dressing laser $\boldsymbol{E}_3$ frequency detuning Δ_3 at discrete Δ_1.

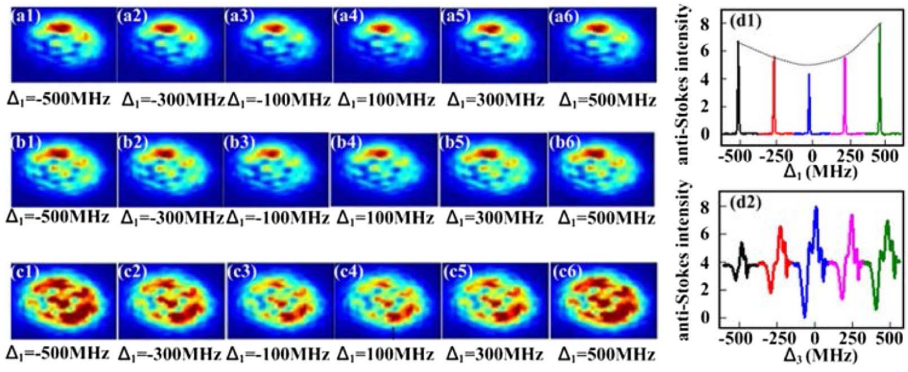

Fig. 6. In PA-SWM process, evolutions of the generated S_1 signal spatial image captured by discretely modifying pumping frequency detuning Δ_1. (a1)–(a6) Rb temperature is set to 60°C; (b1)–(b6) Rb temperature is set to 80°C; (c1)–(c6) Rb temperature is set to 100°C; (d1) frequency spectrum of anti-Stokes versus pumping frequency detuning Δ_1 at discrete $\boldsymbol{E}_4$ frequency detuning; (d2) frequency spectrum of anti-Stokes versus laser $\boldsymbol{E}_3$ frequency detuning Δ_3 at discrete $\boldsymbol{E}_4$ frequency detuning.

into the S_2 photons channel, as expected, the photons of S_1 are amplified. The shapes of S_1 spatial spot images also show a ring centered on the pump beam direction, and these spots tend to form an integral ring with increasing Rb temperature [Figs. 6(a)–6(c)], indicating more spatial modes emerging in the system. Interestingly, the intensity of light spots slightly decreases at a certain pumping frequency ($\Delta_1 = -100$ MHz); then, its intensity increases with the pumping frequency increasing, which is caused by electromagnetically induced absorption (EIA) [26]. This phenomenon is consistent with its spectrum intensity evolutions in the frequency domain, shown by the dashed line in Fig. 6(d1). To further confirm the frequency multimode in the PA-SWM process, an external dressing laser $\boldsymbol{E}_4$ (795 nm) is induced to the inverted Y-type configuration. Figure 6(d2) shows pure dressed S_1 signals versus dressing laser $\boldsymbol{E}_4$ frequency detuning at discrete $\boldsymbol{E}_3$ frequency values. At first sight, the spectrum of S_1 signals shows half dip and half peak, which is consistent with our group's previous theoretical results of dressing suppression and enhancement conditions [27]. In detail, the S_1 further splits into three or more peaks, indicating frequency multimode, which is consistent with the theoretical prediction. Experimentally, the multimode phenomena of SWM are now obvious in both the spatial and spectral domains.

4. CONCLUSION

In conclusion, we have presented a theoretical and experimental study of multimode properties in both frequency and spatial domains by the dressing MWM process. In the spatial domain, multimode behavior is visually demonstrated from the images of the photon fields directly, while in the frequency domain, the anti-Stokes signal spectrum exhibits multi-peaks, indicating the existence of frequency multimode. Dressing laser beams are used to modify the nonlinear susceptibility and then alter the phase-matching condition in the MWM process, thereby increasing the spatial modes and frequency modes. These results will have important applications in quantum imaging.

Funding. National Key RD Program of China (2017YFA0303700, 2018YFA0307500); National Natural Science Foundation of China (11604256, 11804267, 61605154, 61975159, 11904279).

REFERENCES

1. C. Monroe, "Quantum information processing with atoms and photons," Nature **416**, 238–242 (2002).
2. M. Bourennane, M. Eibl, S. Gaertner, C. Kurtsiefer, A. Cabello, and H. Weinfurter, "Decoherence-free quantum information processing with four-photon entangled states," Phys. Rev. Lett. **92**, 107901 (2004).
3. D. P. Caetano, P. H. Souto Ribeiro, J. T. C. Pardal, and A. Z. Khoury, "Quantum image control through polarization entanglement in parametric down-conversion," Phys. Rev. A **68**, 023805 (2003).
4. J. Peřina and J. Křepelka, "Multimode description of stimulated parametric down-conversion," Opt. Commun. **265**, 632–641 (2006).
5. G. Brida, M. Genovese, and I. R. Berchera, "Experimental realization of sub-shot-noise quantum imaging," Nat. Photonics **4**, 227–231 (2010).
6. D. Töyrä, D. D. Brown, M. Davis, S. Song, A. Wormald, J. Harms, H. Miao, and A. Freise, "Multi-spatial-mode effects in squeezed-light enhanced interferometric gravitational wave detectors," Phys. Rev. D **96**, 022006 (2017).
7. C. S. Embrey, M. T. Turnbull, P. G. Petrov, and V. Boyer, "Observation of localized multi-spatial-mode quadrature squeezing," Phys. Rev. X **5**, 031004 (2015).
8. O. Jedrkiewicz, Y. K. Jiang, E. Brambilla, A. Gatti, M. Bache, L. A. Lugiato, and P. Di Trapani, "Detection of sub-shot-noise spatial correlation in high-gain parametric down conversion," Phys. Rev. Lett. **93**, 243601 (2004).
9. F. Devauxa and E. Lantz, "Spatial and temporal properties of parametric fluorescence around degeneracy in a type I LBO crystal," Eur. Phys. J. D **8**, 117–124 (2000).
10. M. Martinelli, N. Treps, S. Ducci, S. Gigan, A. Maitre, and C. Fabre, "Experimental study of the spatial distribution of quantum correlations in a confocal optical parametric oscillator," Phys. Rev. A **67**, 023808 (2002).
11. V. Boyer, A. M. Marino, and P. D. Lett, "Generation of spatially broadband twin beams for quantum imaging," Phys. Rev. Lett. **100**, 143601 (2008).
12. Y. Fang, J. Feng, L. Cao, Y. Wang, and J. Jing, "Experimental implementation of a nonlinear beam splitter based on a phase-sensitive parametric amplifier," Appl. Phys. Lett. **108**, 131106 (2016).
13. Z. Qin, L. Cao, and J. Jing, "Experimental characterization of quantum correlated triple beams generated by cascaded four-wave mixing processes," Appl. Phys. Lett. **106**, 211104 (2015).
14. C. Liu, J. Jing, Z. Zhou, R. C. Pooser, F. Hudelist, L. Zhou, and W. Zhang, "Realization of low frequency and controllable bandwidth squeezing based on a four-wave-mixing amplifier in rubidium vapor," Opt. Lett. **36**, 2979–2981 (2011).
15. C. F. McCormick, V. Boyer, E. Arimondo, and P. D. Lett, "Strong relative intensity squeezing by four-wave mixing in rubidium vapor," Opt. Lett. **32**, 178–182 (2007).
16. S. Du, J. Wen, M. H. Rubin, and G. Y. Yin, "Four-wave mixing and biphoton generation in a two-level system," Phys. Rev. Lett. **98**, 053601 (2007).
17. D. Zhang, C. Li, Z. Zhang, Y. Zhang, Y. Zhang, and M. Xiao, "Enhanced intensity-difference squeezing via energy-level modulations in hot atomic media," Phys. Rev. A **96**, 043847 (2017).
18. K. Bencheikh, E. Huntziger, and J. A. Levenson, "Quantum noise reduction in quasi-phase-matched optical parametric amplification," J. Opt. Soc. Am. B **12**, 847–852 (1995).
19. Z. Nie, H. Zheng, P. Li, Y. Yang, Y. Zhang, and M. Xiao, "Interacting multiwave mixing in a five-level atomic system," Phys. Rev. A **77**, 063829 (2008).
20. J. Wen, S. Du, Y. Zhang, M. Xiao, and M. H. Rubin, "Nonclassical light generation via a four-level inverted-Y system," Phys. Rev. A **77**, 033816 (2008).
21. C. Shu, P. Chen, T. K. A. Chow, L. Zhu, Y. Xiao, M. M. T. Loy, and S. Du, "Subnatural-linewidth biphotons from a Doppler-broadened hot atomic vapour cell," Nat. Commun. **7**, 12783 (2016).
22. M. H. Rubin and Y. Shih, "Resolution of ghost imaging for nondegenerate spontaneous parametric down-conversion," Phys. Rev. A **78**, 033836 (2008).
23. N. V. Corzo, A. M. Marino, K. M. Jones, and P. D. Lett, "Noiseless optical amplifier operating on hundreds of spatial modes," Phys. Rev. Lett. **109**, 043602 (2012).
24. Y. Zhang, Z. Nie, Z. Wang, C. Li, F. Wen, and M. Xiao, "Evidence of Autler–Townes splitting in high-order nonlinear processes," Opt. Lett. **35**, 3420–3424 (2010).
25. X. Li, D. Zhang, M. Sun, K. Li, Z. Wang, and Y. Zhang, "Multi-dressing suppression and enhancement and all-optical switching in parametrically amplified four-wave mixing," Eur. Phys. Lett. **122**, 14005 (2018).
26. A. M. Akulshin, S. Barreiro, and A. Lezama, "Electromagnetically induced absorption and transparency due to resonant two-field excitation of quasidegenerate levels in Rb vapor," Phys. Rev. A **57**, 2996–3002 (1998).
27. P. Li, H. Zheng, Y. Zhang, J. Sun, C. Li, G. Huang, Z. Zhang, Y. Li, and Y. Zhang, "Controlling the transition of bright and dark states via scanning dressing field," Opt. Mater. **35**, 1062–1070 (2013).